Theoretical Rationalization of the Dual Photophysical Behavior of C_{60}^{+}

*Jordi Soler, Rudraditya Sarkar, Martial Boggio-Pasqua**

Laboratoire de Chimie et Physique Quantiques, UMR 5626, IRSAMC, CNRS et Université Toulouse 3, 118 route de Narbonne, 31062 Toulouse, France

ABSTRACT. Interest in fullerenes has been renewed recently in astrophysics as a consequence of their detection in circumstellar environments. In particular, C_{60}^{+} was detected in the diffuse interstellar medium and its presence has been related to some diffuse interstellar bands (DIBs) whose origin was previously unknown. A single recent laboratory experiment (*J. Phys. Chem. A* **2017**, *121*, 7356–7361) shows that upon laser excitation at 785 nm, C_{60}^{+} in neon matrices exhibits a radiative decay at 965 nm, while UV photoexcitation does not lead to any significant luminescence. To rationalize this original dual photophysical behavior, we have performed time-dependent density functional theory (TD-DFT) calculations on C_{60}^{+} to investigate the potential energy surfaces of the relevant electronic states, completed by the simulations of vibrationally-resolved absorption and emission spectra. The proposed photophysical pathways shed light on the experimental measurements: The near-IR laser excitation populates the eleventh doublet excited state (D_{11}) that decays to the lowest first bright excited state D_5, from which photoluminescence is predicted. Indeed, D_5 is largely separated from the lower electronic states (D_0-D_4). Thus, D_5 behaves effectively as the first excited state, while the D_0-D_4 set of states act as the electronic

ground state. In addition, there are no low-lying conical intersections between D_5 and lower excited states energetically accessible upon near-IR excitation that can provide efficient nonradiative decay channels for this state, leaving radiative decay as the most likely deactivation pathway. However, a sloped conical intersection between D_5 and D_4 was located around 2.9 eV above D_0. While it is too high in energy to be accessible upon near-IR excitation, it provides a funnel for efficient nonradiative decay down to the ground state (D_0) accessible upon UV light excitation. Thus, the photophysics of C_{60}^+ is controlled by the ability to access this funnel: Upon near-IR excitation, the system fluoresces because the funnel for nonradiative decay cannot be reached, while UV irradiation provides a different route by opening up a radiationless decay channel via this funnel accounting for the absence of fluorescence.

INTRODUCTION

Fullerenes are fascinating carbon allotropes which are used in a large amount of applications in nanotechnology, material sciences, electronics and biomedicine.[1,2,3,4,5,6,7,8] In addition, these molecules have important implications in astrophysics. Like polycyclic aromatic hydrocarbons (PAHs), these carbonaceous species are believed to be present in the interstellar medium (ISM) and responsible for the observation of diffusive interstellar bands (DIBs).[9,10,11,12] Not surprisingly then, fullerenes have attracted considerable interest both in astronomy and in astrophysics research fields. One major breakthrough came with the assignment of previously unidentified DIBs[13] to the C_{60}^+ radical cation.[14,15,16,17] The buckminsterfullerene cation has thus motivated numerous laboratory measurements of its optical absorption spectra.[16,18,19,20,21,22,23] However, no information about the photophysics of C_{60}^+ had been reported until a very recent laboratory experiment investigated the photoluminescence of this cation.[24] The luminescence measurements show that

C_{60}^+ trapped in a neon matrix at 5 K emits in the near-infrared (NIR) region at 964.5 nm upon excitation in the NIR at 785 nm but no detectable luminescence is obtained upon UV excitation at 405 and 375 nm. This study thus suggests to look for the characteristic NIR emission features of C_{60}^+ in astronomical environments, where either C_{60}/C_{60}^+ has already been detected or fullerenes are likely to be present.

The photophysical behavior observed for C_{60}^+ differs substantially from the one of small compact PAH cations (e.g., naphthalene, anthracene and pyrene) for which ultrafast nonradiative decay is observed[25] and explained by the presence of easily accessible low-lying sloped conical intersections.[26,27,28] The only known PAH cation displaying a similar emissive behavior is the perylene radical cation[29,30] for which no low-lying conical intersection is accessible[31] accounting for the observed luminescence in this cation. It is therefore important to provide a consistent mechanistic picture for the photophysics of this type of system. To do this, it is necessary to understand the excited-state mechanisms involved in the photophysical processes such as ground-state regeneration either by nonradiative decay or photon emission. Very useful insights can be obtained from quantum chemical calculations exploring the potential energy surfaces (PESs) of the relevant electronic states involved in these photophysical processes. In particular, the identification of the excited-state minimum corresponding to the luminescent species and the location of PES crossings, i.e., minimum energy conical intersections (MECIs) that provide ultrafast nonradiative decay channels, are paramount to the rationalization of such photophysical behavior. This type of study has already been conducted for small planar radical cations such as benzene,[32] naphthalene,[26] pyrene[28] and perylene,[31] but to our knowledge, it has never been attempted on the buckminsterfullerene radical cation. The aim of this study is to present a photophysical mechanism for C_{60}^+ that rationalizes the experimental evidence, i.e. the observed photoluminescence upon NIR excitation and the absence of radiative decay upon UV excitation of C_{60}^+, based on the exploration of relevant potential energy surfaces with reliable quantum chemical calculations. After a short presentation of the computational strategy, we first discuss the absorption spectra computed with two different approaches. Then, we identify the species believed to be responsible for the observed NIR emission and compare the simulated vibrationally-resolved emission spectrum with the experimental one. Finally, we propose a simple explanation for the absence of photoluminescence upon UV excitation and summarize the mechanism for the photophysics of C_{60}^+ in conclusion.

COMPUTATIONAL DETAILS

The ground state (D_0) calculations were performed using density functional theory (DFT) in an unrestricted self-consistent field formalism, while time-dependent-DFT (TD-DFT) was used to compute the electronic excited states. The UHF wavefunction stability was checked for D_0. TD-DFT has become a very efficient tool to investigate excited-state processes and to model optical spectra of large systems,[33,34] otherwise not feasible with accurate wave function-based ab initio methods. Errors for vertical transition energies of valence states are typically in the order of 0.25 eV with hybrid functionals.[35] The standard B3LYP functional[36,37] was used throughout this study. This functional provides reliable structures and accurate transition energies for the perylene cation, with C–C bond lengths and transition energies not exceeding 0.016 Å and 0.2 eV deviations, respectively, of the restricted active space self-consistent field (RASSCF) results.[31] It has also been largely used to study the optical properties of PAH cations.[38,39] In addition, the D_0 PES topology of C_{60}^+ was also investigated with B3LYP.[40] The 6-31G* orbital basis set[41,42] was chosen as it includes polarization *d*-functions on the carbon atoms and it has been shown to be flexible enough to give a good qualitative description of the covalent excited states of organic molecules.

The ground-state (D_0) geometry optimization was performed using the appropriate D_{5d} symmetry,[40,43] while the excited-state (D_5) geometry optimization was carried out starting from a slightly distorted D_0 minimum structure without any symmetry restrictions first. When symmetry was recognized, subsequent geometry optimizations were performed with the appropriate symmetry constraints. Numerical frequency calculations were then evaluated within the harmonic approximation to determine the nature of the stationary points found on the respective PESs (i.e., minima vs. saddle points). PES crossings between relevant excited states were optimized without symmetry restrictions at the TD-DFT level using a penalty-constrained algorithm. Here again, the geometry optimization was refined using symmetry constraints upon detection of symmetry point groups.

Vertical transition energies have been computed at the D_0 optimized structure considering up to 80 states. Vibrationally-resolved absorption and emission spectra were simulated in the framework of the Franck-Condon[44] (FC) and nuclear ensemble[45] (NE) approaches. The two methods differ in the way vibrational contributions are taken into account. Within the FC principle, the optimized geometries and normal mode analysis are required for both the initial (i.e., ground-state minimum for absorption and excited-state minimum for emission) and final (i.e., excited-state minimum for absorption and ground-state minimum for emission) states. As mentioned above, these data are obtained from DFT and TD-DFT calculations. The electronic transition dipole moment between the initial and final states is considered to be a constant and the vibronic spectrum results mainly from the calculation of overlap integrals (known as FC integrals) between the vibrational harmonic wave functions of the electronic states involved in the transition. For the NE simulation, these overlap integrals are not explicitly computed. Only the optimized geometry and normal mode analysis of the initial state is needed as input. A number of nonequilibrium geometries are produced and, for each structure, a single point TD-DFT calculation is performed, providing transition energies and electronic transition dipole moments. The spectrum is then integrated over these distinct vertical absorptions. In this way, the spectral band shape results mainly from the initial-state nuclear geometry distribution. For both methods, a phenomenological Gaussian broadening was used to account for the convolution of the spectral lines. This factor was chosen to visually reproduce the experimental band shapes. In the NE simulations, an ensemble of 240 geometries were prepared and the first fifteen excited states were considered for simulating the absorption spectrum in the spectral range of interest ($\lambda > 785$ nm, the excitation wavelength). This spectrum was simulated varying the number of nonequilibrium geometries to test the convergence of the results (Figure S1 in Supp. Info.). For the FC absorption spectrum, only the D_5 state was considered, as no minimum on the D_6 PES could be located. For the NE emission spectrum, only the D_5 state was considered to contribute to the emission at very low temperature and the spectrum was generated using the same number of sampling geometries. All spectra were simulated at 0 K.

DFT and TD-DFT calculations, including geometry optimizations of stationary points and harmonic frequency analyses, were performed with Gaussian09.[46] This program was also used for the FC simulations. Q-Chem 5.0[47] was used to perform the MECI optimizations. The NE simulations were carried out using the software Newton-X.[48]

RESULTS AND DISCUSSION

Ground-State Structure and Absorption Spectrum. It is well known that the neutral buckminsterfullerene C_{60} has a ground-state structure belonging to the icosahedral symmetry.[49]

After removal of an electron from the fivefold degenerate highest occupied molecular orbital (HOMO) of the h_u irreducible representation, the resulting radical cation is stabilized due to Jahn-Teller effects leading to a species with reduced D_{5d} symmetry.[40,43] Our D_0 geometry optimization along with the harmonic frequency analysis confirm that the ground-state structure corresponds to a minimum of D_{5d} symmetry with a $^2A_{1u}$ electronic configuration. The singly occupied molecular orbital (SOMO) is the delocalized π-MO $6a_{1u}$ shown in Figure 1.

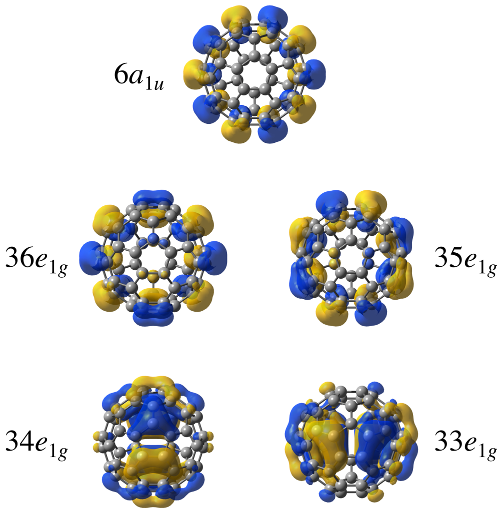

Figure 1. Relevant molecular orbitals for C_{60}^+ at its minimum D_0 structure of D_{5d} symmetry.

The lowest thirteen doublet excited states are mainly obtained by π–π electronic transitions from the thirteen lowest lying π-MOs to the $6a_{1u}$ SOMO (see Table 1). The higher excited states above D_{13} are due to π–π* transitions. Vertical transition energies for the lowest thirteen doublet excited states are provided in Table 1. It shows that the excited states D_1 to D_4 are close in energy to D_0. This is not surprising as the D_0-D_4 set of states all arise from the fivefold degenerate ^1H_u state of the neutral C_{60}. The first bright state is D_5 and is degenerate with D_6. The excitation energy between D_0 and D_5/D_6 is 1.39 eV (892 nm). The second state with a non-zero oscillator strength (f) is also a degenerate state (D_{11}/D_{12}) with an excitation energy of 1.55 eV (801 nm), but this state is 16 times less intense than the D_5/D_6 pair of states. Since no other bright state has an energy close to the experimental laser excitation at 785 nm, we expect that this NIR laser excitation is actually populating D_{11}/D_{12} pair of states.

Table 1. Lowest thirteen vertical transition energies computed at TD-DFT/6-31G* level at the minimum D_0 structure of D_{5d} symmetry.

Transitions	States	ΔE (eV)	λ (nm)	*f*
$36e_{1u}\rightarrow 6a_{1u}$	D_1	0.206	6032	0.000
$35e_{1u}\rightarrow 6a_{1u}$	D_2	0.206	6032	0.000
$36e_{2u}\rightarrow 6a_{1u}$	D_3	0.208	5974	0.000
$35e_{2u}\rightarrow 6a_{1u}$	D_4	0.208	5974	0.000
$36e_{1g}\rightarrow 6a_{1u}$	D_5	1.391	892	0.032
$35e_{1g}\rightarrow 6a_{1u}$	D_6	1.391	892	0.032
$36e_{2g}\rightarrow 6a_{1u}$	D_7	1.514	819	0.000
$35e_{2g}\rightarrow 6a_{1u}$	D_8	1.514	819	0.000
$34e_{2g}\rightarrow 6a_{1u}$	D_9	1.537	807	0.000
$33e_{2g}\rightarrow 6a_{1u}$	D_{10}	1.537	807	0.000
$34e_{1g}\rightarrow 6a_{1u}$	D_{11}	1.548	801	0.002
$33e_{1g}\rightarrow 6a_{1u}$	D_{12}	1.548	801	0.002
$14a_{1g}\rightarrow 6a_{1u}$	D_{13}	1.572	789	0.000

Figure 2 provides the simulated absorption spectrum using the NE approach based on the lowest fifteen excited states and a comparison between the FC and NE formalisms for the high-resolution spectrum in the NIR spectral range is presented in the inset. The absorption spectrum shows two intense bands in the 900-1000 nm range attributed to the $D_0 \rightarrow D_5$ and $D_0 \rightarrow D_6$ transitions. The experimental excitation energy at 785 nm coincides with the $D_0 \rightarrow D_{11}$ and $D_0 \rightarrow D_{12}$ transitions. Comparing the simulated high-resolution NIR absorption spectra with the recorded experimental absorption spectrum of C_{60}^+ in the gas phase,[15] the two observed absorption bands at 963.2 nm and 957.7 nm are well reproduced by our simulations with peaks at 959 nm and 951 nm for the NE spectrum and peaks at 958 nm and 950 nm for the FC spectrum. This is also in good agreement with the absorption spectrum of C_{60}^+ trapped in a neon matrix at 5 K.[24] Note that the relative intensity of these two peaks is in better agreement with the NE simulated spectrum (compare with Figure 3b in Ref. [24]). This is probably due to the fact that in the FC simulated spectrum the absorption only results from the $D_0 \rightarrow D_5$ transition (with a total spectral progression of the simulated spectrum reaching ~94%), while the NE spectrum also includes contributions from $D_0 \rightarrow D_6$. We expect therefore a more accurate description of the absorption spectrum with the NE approach, as both D_5 and D_6 strongly contribute to the absorption of C_{60}^+ in the NIR range. This could also possibly explain the better agreement with the next absorption peaks observed between 910-930 nm in Ref. [24].

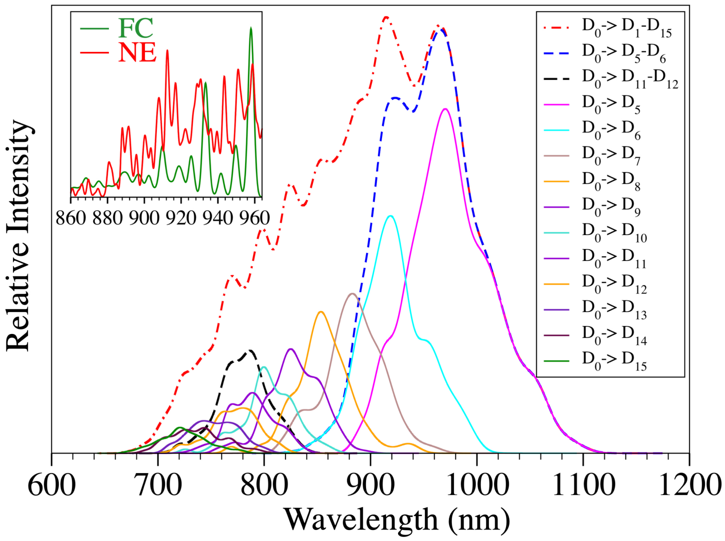

Figure 2. Convoluted absorption spectrum of C_{60}^+ and spectrum decomposition simulated using the first fifteen excited states within the NE approach (see Figure S2 in Supp. Info. for the error due to the statistical sampling). The inset shows the high-resolution absorption spectrum in the NIR region with the FC (green line) and NE (red line) approaches.

Near-IR Photoluminescence. Because the experimental NIR laser excitation at 785 nm used is in good agreement with the $D_0 \rightarrow D_{11}/D_{12}$ transition energy (see Table 1 and Figure 2), we assume that the initial photoexcited states are D_{11}/D_{12}. As shown in Table 1, the energy gaps with lower electronic states down to D_5 are pretty small with all the states from D_5 to D_{12} found within 0.16 eV. Then, a large energy gap is found with the next lower excited state D_4, with a D_5–D_4 energy gap of 1.18 eV. Thus, D_5 can be considered effectively as "D_1", while the D_0-D_4 set of states play the effective role of "D_0". As a consequence, we expect efficient nonradiative decay to take place from the initially excited D_{11}/D_{12} states down to D_5, from which luminescence is expected to take place, provided no easily accessible conical intersections are available for efficient nonradiative decay from D_5. To verify this scenario, we have optimized the D_5 structure and searched for D_5/D_4

MECIs. At the end of the D_5 geometry optimization, the excited radical cation has no longer D_{5d} symmetry because an electron has been removed from a degenerate e_{1g} MO and, as a consequence of a Jahn-Teller instability, the symmetry is reduced to C_i. This Jahn-Teller effect is rather weak with a relaxation energy in the D_5 state between the D_{5d} and C_i structures of 0.063 eV and C–C bond lengths modifications not exceeding 0.02 Å. At this D_5 minimum geometry, the vertical emission energy is computed at 1.242 eV, corresponding to an emission wavelength of 999 nm, in good agreement with the experimental value of 964.5 nm[24] (963.2 nm in the gas phase[15]). An excellent agreement is obtained when considering the 0–0 transition energy, which is computed at 1.294 eV (958 nm). Note that this agreement is beyond expectation, as typical errors for TD-DFT transition energies are typically within 0.3 eV for covalent singly-excited transitions. In addition, a D_5/D_4 MECI was located at an energy above that provided by NIR excitation (see next subsection), making this funnel for nonradiative decay not accessible.

Figure 3 shows the vibrationally-resolved emission spectra computed both with FC and NE approaches. The FC simulated emission spectrum displays the most intense band exactly at the 0–0 transition, in agreement with the experimental observations.[15,24] A second less intense emission band is observed shifted by 265 cm^{-1} to lower energy with respect to the 0–0 transition, in very good agreement with the experimental spectrum,[24] which shows a secondary band at 262 cm^{-1} at lower energies. This band was assigned experimentally to the first vibrationally excited level of the electronic ground state, corresponding to a radial a_{1g} vibrational mode of C_{60}^+. Our FC simulation confirms this assignment from the analysis of the vibrational progression. This a_{1g} vibrational mode at 267 cm^{-1} corresponds to a breathing motion of C_{60}^+ with a contraction along one direction of the ball and an expansion along two orthogonal directions (see animated movie in Supp. Info.). The NE spectrum is slightly red-shifted (by 423 cm^{-1}) compared to the FC spectrum.

However, the spectrum envelop reproduces very nicely the experimental one, with two shoulders occurring at higher energies than the 0–0 maximum.

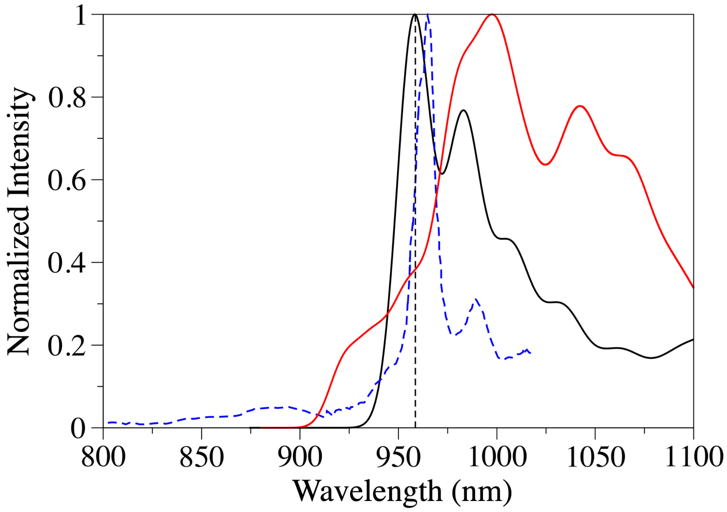

Figure 3. Simulated emission spectra of C_{60}^{+} within the FC (black line) and NE (red line) approaches. The vertical dashed line marks the computed 0–0 transition. The dashed blue line is the experimental spectrum digitalized from Ref. [24].

UV Photostability. Unlike the NIR photophysical pathway which leads to radiative decay, UV excitation at 405 and 375 nm does not lead to any detectable fluorescence.[24] Although we have computed up to 80 vertical transition energies, the excited states with an excitation wavelength lower than 500 nm suffer from a large spin contamination and are thus unreliable. Based on our TD-DFT calculations, it is therefore not possible to identify the electronic states that are initially populated by these UV excitations. However, due to the high density of electronic states in that region of the spectrum, it can be assumed that efficient nonradiative decay will take place down to the D_5 state, in a similar way that we have assumed efficient decay from D_{11} to D_5 in NIR photophysical pathway. Of course, upon UV excitation, the D_5 state produced will have a lot more vibrational kinetic energy available.

To account for the lack of luminescence from D_5 upon UV excitation, we have searched for MECIs between D_5 and D_4. If such a crossing exists and is energetically accessible, then it would provide a nonradiative decay path that would be responsible for luminescence quenching. As explained in the previous subsection, we found a D_5/D_4 MECI. It that has a C_i symmetry structure like the D_5 minimum structure. It is located 2.869 eV above the ground state D_{5d} minimum and 1.541 eV above the D_5 excited-state C_i minimum. The high activation energy necessary to reach this MECI from the D_5 minimum is the result of substantial structural deformations involving changes in the C–C bond lengths up to 0.08 Å. Because the UV excitation at 405 nm and 375 nm provides 3.061 eV and 3.306 eV above D_0, respectively, whereas the NIR excitation at 785 nm only provides 1.579 eV, this D_5/D_4 MECI is unreachable upon NIR excitation but becomes energetically accessible upon UV excitation. Thus, our results suggest that the hot D_5 state produced upon UV irradiation has enough vibrational kinetic energy available to access this funnel for nonradiative decay down to D_4. The topology of this MECI is sloped[50,51] (Figure S3 in Supp. Info.) and will favor the photostabilization[26,28,52,53] of C_{60}^+. Following UV excitation and radiationless decay to D_4, the system can easily relax down to D_0, as the D_0-D_4 manifold of states are coupled via the symmetry-enforced (Jahn-Teller) icosahedral conical intersection.

CONCLUSION

The present theoretical investigation described two distinct photophysical pathways corresponding to NIR and UV irradiation of C_{60}^+, respectively. These pathways are schematically summarized in Figure 4. In the first case, C_{60}^+ is fluorescent in the NIR range. Upon excitation to the D_{11} excited state, the system can decay nonradiatively to the lower D_5 excited state, which has been identified as the electronic state responsible for the observed emission. The predicted fluorescence maximum (at 0 K) is attributed to the 0–0 transition between the D_5 and D_0 states and computed at 958 nm, in excellent agreement with the experimental 0–0 transition values of 964.5 nm in a Ne matrix at 5 K and 963.2 nm in the gas phase at 5.8 K. The vibrationally-resolved emission spectra reproduce beautifully the band structures of the experimental fluorescence spectrum, in particular the second most intense band shifted by 265 cm^{-1} to lower energies, which is assigned to the first vibrational excited state of a radial a_{1g} normal mode of C_{60}^+. In the case of UV irradiation, C_{60}^+ is excited to higher excited states that are assumed to decay rapidly to the lower D_5 state. The excess of vibrational kinetic energy available is then sufficient to access a sloped D_5/D_4 MECI responsible for the internal conversion to D_4. This state can then decay down to D_0 via interstate couplings in the region of the symmetry-induced conical intersection found in the icosahedral symmetry.

To summarize, the photophysics of C_{60}^+ is controlled by the accessibility of a sloped conical intersection. Upon NIR excitation this crossing is not accessible and the system decays radiatively, whereas upon UV excitation this funnel allows for efficient nonradiative decay back to the ground electronic state of C_{60}^+. This simple mechanistic picture provides a rationale behind the experimental observations. These findings may be interesting to astrophysicists who are looking for the origin of some diffuse interstellar bands and of unidentified IR emission bands observed in the interstellar medium.

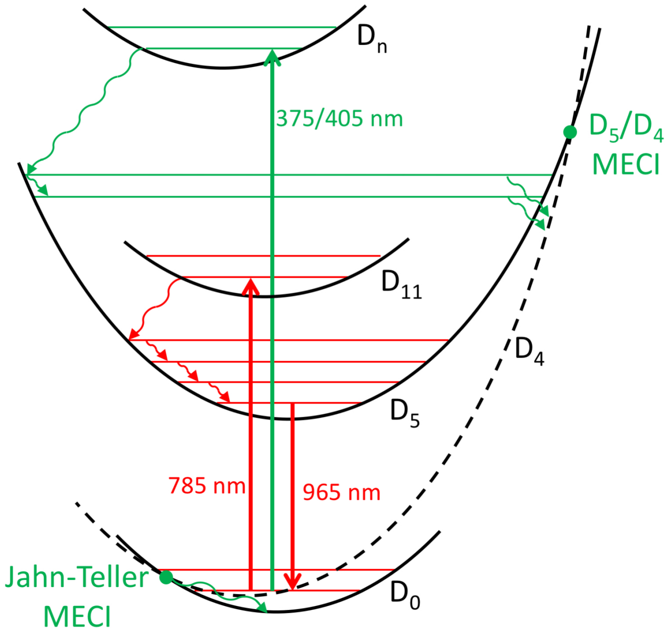

Figure 4. Schematic representation of the NIR radiative (in red) and of the UV nonradiative (in green) photophysical pathways.

ASSOCIATED CONTENT

Supporting Information. The following files are available free of charge. Tables S1-S3 for the Cartesian coordinates of all the optimized structures. Figure S1 for the effect of the number of sampling geometries on the simulated NE absorption spectrum. Figure S2 for the error due to the statistical sampling for the simulated NE absorption spectrum reported in Figure 2. Figure S3 for the D_4 and D_5 gradients at the D_5/D_4 MECI. (PDF file) A movie file showing the radial a_{1g} vibrational mode of C_{60}^+. (GIF file)

AUTHOR INFORMATION

Corresponding Author

*Email: martial.boggio@irsamc.ups-tlse.fr

ORCID

Martial Boggio-Pasqua: 0000-0001-6684-5223

Author Contributions

The manuscript was written through contributions of all authors. All authors have given approval to the final version of the manuscript. All authors contributed equally.

Funding Sources

We thank the LABEX NEXT for providing the funding of R. Sarkar's postdoctoral fellowship and the TCCM Scholarship for providing the funding of J. Soler's internship.

Notes

The authors declare no competing financial interest.

ACKNOWLEDGMENTS

This work was granted access to the HPC resources of CALMIP supercomputing center under the allocation 2018-[12158].

REFERENCES

---

[1] Thomson, B. C.; Fréchet, J. M. J. Polymer-Fullerene Composite Solar Cells. *Angew. Chem. Int. Ed.* **2008**, *47*, 58–77.

[2] Martín, N.; Giacalone, F. (Eds.), Fullerene Polymers: Synthesis, Properties and Applications. Wiley-VCH Verlag GmbH & Co. KGaA, Weinheim, 2009.

---

[3] Guldi, D. M.; Illescas, B. M.; Atienza, C. M.; Wielopolski, M.; Martín, N. Fullerene for Organic Electronics. *Chem. Soc. Rev.* **2009**, *38*, 1587–1597.

[4] Dennler, G.; Scharber, M. C.; Brabec, C. J. Polymer-Fullerene Bulk-Heterojunction Solar Cells. *Adv. Mater.* **2009**, *21*, 1323–1338.

[5] Lebedeva, M. A.; Chamberlain, T. W.; Khlobystov, A. N. Harnessing the Synergistic and Complementary Properties of Fullerene and Transition-Metal Compounds for Nanomaterial Applications. *Chem. Rev.* **2015**, *115*, 11301–11351.

[6] Kirner, S.; Sekita, M.; Guldi, D. M. 25th Anniversary Article: 25 Years of Fullerene Research in Electron Transfer Chemistry. *Adv. Mater* **2014**, *26*, 1482–1493.

[7] Bakry, R.; Vallant, R. M.; Najam-ul-Haq, M.; Rainer, M.; Szabo, Z.; Huck, C. W.; Bonn, G. K. Medicinal Applications of Fullerenes. *Int. J. Nanomedicine* **2007**, *2*, 639–649.

[8] Goodarzi, S.; Da Ros, T.; Conde, J.; Sefat, F.; Mozafari, M. Fullerene: Biomedical Engineers Get to Revisit an Old Friend. *Mater. Today* **2017**, *20*, 460–480.

[9] Léger, A.; d'Hendecourt, L.; Verstraete, L.; Schmidt, W. Remarkable Candidates for the Carrier of the Diffuse Interstellar bands: C_{60}^+ and Other Polyhedral Carbon Ions. *Astron. Astrophys.* **1988**, 203, 145–148.

[10] Kroto, H. W.; Jura, M. Circumstellar and Interstellar Fullerenes and their Analogues. *Astron. Astrophys.* **1992**, *263*, 275–280.

[11] Cami, J.; Bernard-Salas, J.; Peeters, E.; Malek, S. E. Detection of C_{60} and C_{70} in a Young Planetary Nebula. *Science* **2010**, *329*, 1180–1182.

---

[12] Omont, A. Interstellar Fullerene Compounds and Diffuse Interstellar Bands. *Astron. Astrophys.* **2016**, *590*, A52.

[13] Snow, T. P.; McCall, B. J. Diffuse Atomic and Molecular Clouds. *Annu. Rev. Astron. Astrophys.* **2006**, *44*, 367–414.

[14] Foing, B. H.; Ehrenfreund, P. Detection of Two Interstellar Absorption Bands Coincident with Spectral Features of C_{60}^+. *Nature* **1994**, *369*, 296–298.

[15] Campbell, E. K.; Holz, M.; Gerlich, D.; Maier, J. P. Laboratory Confirmation of C_{60}^+ as the Carrier of Two Diffuse Interstellar Bands. *Nature* **2015**, *523*, 322–323.

[16] Walker, G. A. H.; Bohlender, D.; Maier, J. P.; Campbell, E. K. Identification of More Interstellar C_{60}^+ Bands. *Astrophys. J. Lett.* **2015**, *812*, L8.

[17] Campbell, E. K.; Holz, M.; Maier, J. P.; Gerlich, D.; Walker, G. A. H.; Bohlender, D. Gas Phase Absorption Spectroscopy of C_{60}^+ and C_{70}^+ in a Cryogenic Ion Trap: Comparison with Astronomical measurements. *Astrophys. J.* **2016**, *822*, 17.

[18] Kato, T.; Kodama, T.; Shida, T.; Nakagawa, T.; Matsui, Y.; Suzuki, S.; Shiromaru, H.; Yamauchi, K.; Achiba, Y. Electronic Absorption Spectra of the Radical Anions and Cations of Fullerenes: C_{60} and C_{70}. *Chem. Phys. Lett.* **1991**, *180*, 446–450.

[19] Gasyna, Z.; Andrews, L.; Schatz, P. Near-Infrared Absorption Spectra of Fullerene (C_{60}) Radical Cations and Anions Prepared Simultaneously in Solid Argon. *J. Phys. Chem.* **1992**, *96*, 1525–1527.

[20] Fulara, J.; Jakobi, M.; Maier, J. Electronic and Infrared Spectra of C_{60}^+ and C_{60}^- in Neon and Argon Matrices. *Chem. Phys. Lett.* **1993**, *211*, 227–234.

---

[21] Kern, B.; Strelnikov, D.; Weis, P.; Böttcher, A.; Kappes, M. M. IR Absorptions of C_{60}^+ and C_{60}^- in Neon Matrixes. *J. Phys. Chem. A* **2013**, *117*, 8251−8255.

[22] Kaiser, A.; Postler, J.; Ončák, M.; Kuhn, M.; Renzler, M.; Spieler, S.; Simpson, M.; Gatchell, M.; Beyer, M. K.; Wester, R.; Gianturco, F. A.; Scheier, P.; Calvo, F.; Yurtsever, E. Isomeric Broadening of C_{60}^+ Electronic Excitation in Helium Droplets: Experiments Meet Theory. *J. Phys. Chem. Lett.* **2018**, *9*, 1237–1242.

[23] Campbell, E. K.; Maier, J. P. Isomeric and Isotopic Effects on the Electronic Spectrum of C_{60}^+-He: Consequences for Astronomical Observations of C_{60}^+. *Astrophys. J.* **2018**, *858*, 36.

[24] Strelnikov, D. V.; Kern, B.; Kappes, M. M. Near-IR Photoluminescence of C_{60}^+. *J. Phys. Chem. A* **2017**, *121*, 7356–7361.

[25] Zhao, L.; Lian, R.; Shkrob, I. A.; Crowell, R. A.; Pommeret, S.; Chronister, E. L.; Liu, A. D.; Trifunac, A. D. Ultrafast studies on the photophysics of matrix-isolated radical cations of polycyclic aromatic hydrocarbons. *J. Phys. Chem. A* **2004**, *108*, 25–31.

[26] Hall, K. F.; Boggio-Pasqua, M.; Bearpark, M. J.; Robb, M. A. Photostability via sloped conical intersections: A computational study of the excited states of the naphthalene radical cation. *J. Phys. Chem. A* **2006**, *110*, 13591–13599.

[27] Hall, K. F.; Tokmachev, A. M.; Bearpark, M. J.; Boggio-Pasqua, M.; Robb, M. A. Molecular mechanics-valence bond method for planar conjugated hydrocarbon cations. *J. Chem. Phys.* **2007**, *127*, 134111.

---

[28] Tokmachev, A. M.; Boggio-Pasqua, M.; Bearpark, M. J.; Robb, M. A. Photostability via sloped conical intersections: A computational study of the pyrene radical cation. *J. Phys. Chem. A* **2008**, *112*, 10881–10886.

[29] Joblin, C.; Salama, F.; Allamandola, L. Photoinduced fluorescence from the perylene cation isolated in Ne and Ar matrices. *J. Chem. Phys.* **1995**, *102*, 9743–9745.

[30] Chillier, X. D. F.; Stone, B. M.; Joblin, C.; Salama, F.; Allamandola, L. J. $D_1(^2B_{2g})\rightarrow D_0(^2A_u)$ fluorescence from the matrix-isolated perylene cation following laser excitation into the $D_5(^2B_{3g})$ and $D_2(^2B_{3g})$ electronic states. *J. Chem. Phys.* **2002**, *116*, 5725–5730.

[31] Tokmachev, A. M.; Boggio-Pasqua, M.; Mendive-Tapia, D.; Bearpark, M. J.; Robb, M. A. Fluorescence of the perylene radical cation and an inaccessible D_0/D_1 conical intersection: An MMVB, RASSCF and TD-DFT computational study. *J. Chem. Phys.* **2010**, *132*, 044306.

[32] Applegate, B. E.; Miller, T. A. Calculation of the Jahn-Teller Effect in Benzene Cation: Application to Spectral Analysis. *J. Chem. Phys.* **2002**, *117*, 10654–10674.

[33] Casida, M. E.; Huix-Rotllant, M. Progress in Time-Dependent Density-Functional Theory. *Annu. Rev. Phys. Chem.* **2012**, *63*, 287–323.

[34] Santoro, F.; Jacquemin, D. Going Beyond the Vertical Approximation with Time-Dependent Density Functional Theory. *WIREs Comput. Mol. Sci.* **2016**, *6*, 460–486.

[35] Laurent, A. D.; Jacquemin, D. TD-DFT Benchmarks: A Review. *Int. J. Quantum Chem.* **2013**, *113*, 2019–2039.

[36] Becke, A. D. Density-Functional Thermochemistry. III. The Role of Exact Exchange. *J. Chem. Phys.* **1993**, *98*, 5648–5652.

---

[37] Stephens, P. J.; Devlin, F. J.; Chabalowski, C. F.; Frisch, M. J. Ab Initio Calculation of Vibrational Absorption and Circular Dichroism Spectra Using Density Functional Force Fields. *J. Chem. Phys.* **1994**, *98*, 11623–11627.

[38] Dierksen, M.; Grimme, S. Density Functional Calculations of the Vibronic Structure of Electronic Absorption Spectra. *J. Chem. Phys.* **2004**, *120*, 3544–3554.

[39] Malloci, G.; Mullas, G.; Cappellini, G.; Joblin, C. Time-Dependent Density Functional Study of the Electronic Spectra of Oligoacenes in the charge States –1, 0, +1 and +2. *Chem. Phys.* **2007**, *340*, 43–58.

[40] Muya, J. T.; Ramanantoanina, H.; Daul, C.; Nguyen, M. T.; Gopakumar, G.; Ceulemans, A. Jahn–Teller Instability in Cationic Boron and Carbon Buckyballs B_{80}^+ and C_{60}^+: A Comparative Study. *Phys. Chem. Chem. Phys.* **2013**, *15*, 2829–2835.

[41] Hehre, W. J.; Ditchfield, R.; Pople, J. A. Self-Consistent Molecular Orbital Methods. XII. Further Extensions of Gaussian-Type Basis Sets for Use in Molecular Orbital Studies of Organic Molecules. *J. Chem. Phys.* **1972**, *56*, 2257–2261.

[42] Hariharan, P. C.; Pople, J. A. The Influence of Polarization Functions on Molecular Orbital Hydrogenation Energies. *Theoret. Chim. Acta* **1973**, *28*, 213–222.

[43] Ceulemans, A.; Fowler, P. W. The Jahn–Teller Instability of Fivefold Degenerate States in Icosahedral Molecules. *J. Chem. Phys.* **1990**, *93*, 1221–1234.

[44] Barone, V.; Bloino, J.; Biczysko, M.; Santoro, F. Fully Integrated Approach to Compute Vibrationally Resolved Optical Spectra: From Small Molecules to Macrosystems. *J. Chem. Theory Comput.* **2009**, *5*, 540–554.

---

[45] Crespo-Otero, R.; Barbatti, M. Spectrum Simulation and Decomposition with Nuclear Ensemble: Formal Derivation and Application to Benzene, Furan and 2-Phenylfuran. *Theor. Chem. Acc.* **2012**, *131*, 1237.

[46] Frisch, M. J.; Trucks, G. W.; Schlegel, H. B.; Scuseria, G. E.; Robb, M. A.; Cheeseman, J. R.; Scalmani, G.; Barone, V.; Mennucci, B.; Petersson, G. A.; et al., *Gaussian 09*, revision D.01, Gaussian, Inc., Wallingford CT, 2009.

[47] Shao, Y. S.; Gan, Z.; Epifanovsky, E.; Gilbert, A. T. B.; Wormit, M.; Kussmann, J.; Lange, A. W.; Behn, A.; Deng, J.; Feng, X. et al. Advances in Molecular Quantum Chemistry Contained in the Q-Chem 4 program package. *Mol. Phys.* **2015**, *113*, 184–215.

[48] Barbatti, M.; Ruckenbauer, M.; Plasser, F.; Pittner, J.; Granucci, G.; Persico, M.; Lischka, H. Newton-X: a surface-hopping program for nonadiabatic molecular dynamics. *WIREs Comput. Mol. Sci.* **2014**, *4*, 26–33.

[49] Johnson, R. D.; Meijer, G.; Bethune, D. S. C_{60} Has Icosahedral Symmetry. *J. Am. Chem. Soc.* **1990**, *112*, 8983–8984.

[50] Atchity, G. J.; Xantheas, S. S.; Ruedenberg, K. Potential Energy Surfaces Near Intersections. *J. Chem. Phys.* **1991**, *95*, 1862–1876.

[51] Blancafort, L. Photochemistry and Photophysics at Extended Seams of Conical Intersection. *ChemPhysChem* **2014**, *15*, 3166–3181.

[52] Boggio-Pasqua, M.; Bearpark, M. J.; Robb, M. A. Photostability via a Sloped Conical Intersection: a CASSCF and RASSCF Study of Pyracylene. *J. Phys. Chem. A* **2005**, *109*, 8849–8856.

---

[53] Tuna, D.; Sobolewski, A. L.; Domcke, W. Conical-Intersection Topographies Suggest That Ribose Exhibits Enhanced UV Photostability. *J. Phys. Chem. B* **2016**, *120*, 10729–10735.

TOC Graphic.

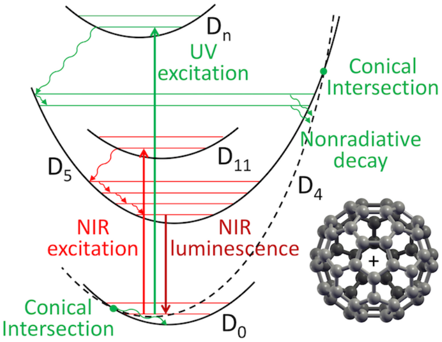
D_n
UV excitation
Conical Intersection
Nonradiative decay
D_{11}
D_5
D_4
NIR excitation
NIR luminescence
Conical Intersection
D_0
+